# 7 Elastic Contact

In this chapter, we consider a nonconforming approach for the elastic contact between deformable bodies with and without friction. We follow the lines of [KW00, KW01], in particular [KW01], and we discuss a nonlinear Dirichlet–Neumann algorithm. No penetration between the bodies occurs but free tangential displacement is permitted, at least in case of frictionless contact. The resulting algorithm leads to an efficient solver of the arising discrete system. Moreover, even for a small number of unknowns the computed discrete boundary stresses are highly accurate. For simplicity, we restrict ourselves to the case of two deformable bodies in contact.

The main difficulty when numerically solving contact problems involving two or more bodies is the information transfer at the interface, since, in general, one can not expect the meshes at the interface to match. To obtain a stable and optimal discretization scheme for the global problem, the information transfer and the communication between the subdomains is of crucial importance. Different strategies, e.g., creating point-point or element-point correlations, are known, see [Wri95] for a survey. Here, we follow an approach based on the weak formulation of the contact problem. The interface coupling is realized in terms of a weak continuity condition, i.e., in terms of Lagrange multipliers. Our discretization scheme is based on mortar techniques [BMP93, BMP94]. Originally introduced as a domain decomposition method for the coupling of spectral elements, these techniques are used in a large class of nonconforming situations. Thus, the coupling of different physical models, discretization schemes, or non-matching triangulations along interior interfaces of the domain can be analyzed by mortar methods. These domain decomposition techniques provide a more flexible approach than standard conforming formulations.

This chapter is structured as follows. In a first step, we state the problem of frictionless elastic contact and give it's weak formulation. We explain the discretization used. Here, we put particular emphasis on the information transfer between the two deformable bodies, which is realized in terms of a scaled mass matrix arising from a dual Lagrange multiplier space. In Section 7.1, we present the nonlinear Dirichlet–Neumann algorithm. This Algorithm is used to solve the arising discrete system. In each step of the nonlinear Dirichlet–Neumann algorithm, we have to solve a linear problem and a nonlinear one–sided contact problems. This is done using a standard multigrid method and our monotone multigrid method for contact problems, respectively. Numerical examples illustrating the performance of the method are given in Section 7.2. In Section 7.3, we consider teh elastic contact of two bodies with Coulomb friction. The Dirichlet Neumann algorithm is generalized to the case of frictional contact. Finally, in Section 7.4, we give numerical results. Let us point out, that the resulting method shows to be efficient and highly accurate. This demonstrated by giving several numerical examples.

We point out, that for notational convenience we drop any level indices in this chapter. Furthermore, we have to redefine certain quantities as the bilinearform $a(\cdot,\cdot)$ or the convex set of admissible displacements $\mathcal{K}$. The two bodies in their reference configuration are identified with the domains $\mathcal{B}_k \subset \mathbb{R}^d$, $k = 1, 2$, $d = 2, 3$, and we decompose the solution $\boldsymbol{u}$ in $\boldsymbol{u} = (\boldsymbol{u}_1, \boldsymbol{u}_2)$, and write $(\boldsymbol{u}_k)_n := \boldsymbol{u}_k \cdot \boldsymbol{n}_k$, $k = 1, 2$, where $\boldsymbol{n}_k$ is the outer unit normal on $\partial\mathcal{B}_k$. By definition, the Lagrange multiplier is defined on the non-mortar side.

Here, we associate the non-mortar side with subdomain $\mathcal{B}_1$. Let us start with the case of frictionless contact. Following the lines of Chapter 2, we decompose the boundary of $\mathcal{B}$ into three disjoint parts, $\Gamma_D$ is the Dirichlet part, $\Gamma_N$ denotes the Neumann part and $\Gamma_S$ stands for the contact boundary. The actual contact zone between the two bodies is a priori unknown and is assumed to be a subset of $\Gamma_S$. In addition to the equilibrium conditions in $\mathcal{B}_1$ and $\mathcal{B}_2$ and the boundary conditions on $\partial\mathcal{B}$, see Chapter 1, we have the following conditions on the possible contact boundary $\Gamma_S$

$$\begin{array}{rcccl} \boldsymbol{\sigma}_T(\boldsymbol{u}_1) & = & \boldsymbol{\sigma}_T(\boldsymbol{u}_2) & = & 0 \ , \\ \sigma_n(\boldsymbol{u}_1) & = & \sigma_n(\boldsymbol{u}_2) & \leq & 0 \ , \end{array} \tag{7.1}$$

and the linearized contact condition on $\Gamma_S$

$$\begin{array}{rcl} t & \geq & (\boldsymbol{u}_1)_n + (\boldsymbol{u}_2)_n \ , \\ 0 & = & ((\boldsymbol{u}_1)_n + (\boldsymbol{u}_2)_n - t)\, \sigma_n(\boldsymbol{u}_1) \ , \end{array} \tag{7.2}$$

where the function $t\colon \Gamma_S \subset \mathbb{R}^d \longrightarrow \mathbb{R}$ is the distance between the two bodies in normal direction taken with respect to the reference configuration, see [HH80, BGK87]. We assume that $t$ is continuous. The interpretation of the boundary conditions (7.1) is similar to that given in Chapter 2. As in the case of Signorinis problem, we assume frictionless contact. Thus, the tangential stresses vanish at the contact boundary, and are set to zero in the first equation of (7.1). We have only contact pressure at $\Gamma_S$. If there is no contact between the two bodies, the boundary stresses at $\Gamma_S$ are zero, see (7.1) and (7.2).

In this chapter, the bilinear form $a(\cdot,\cdot)$ is given by

$$a(\boldsymbol{v},\boldsymbol{w}) := \sum_{k=1}^{2} \int_{\mathcal{B}_k} H_{ijlm} w_{i,j} v_{l,m}\, dx, \quad \boldsymbol{w},\boldsymbol{v} \in \prod_{k=1}^{K} \boldsymbol{H}^1(\mathcal{B}_k) \ ,$$

where Hooke's tensor $H_{ijlm}$ is assumed to be constant on each subdomain and $\boldsymbol{H}^1(\mathcal{B}_k) := (H^1(\mathcal{B}_k))^d$. We write $f(\boldsymbol{v}) := (\boldsymbol{v},\boldsymbol{f})_{\boldsymbol{L}^2(\mathcal{B})} + (\boldsymbol{v},\boldsymbol{p})_{\boldsymbol{L}^2(\Gamma_N)}$ and denote by $f_k(\cdot)$ and $a_k(\cdot,\cdot)$ the restriction of $f(\cdot)$ and $a(\cdot,\cdot)$ to $\mathcal{B}_k$, $k = 1, 2$, respectively.

As it is the case for Signorini's problem, the weak solution of the nonlinear contact problem can be obtained by a minimization problem on a convex set $\mathcal{K}$. We define the convex set $\mathcal{K}$ of admissible displacements by

$$\mathcal{K} = \{\boldsymbol{v} \in \boldsymbol{H}^1_*(\mathcal{B}_1) \times \boldsymbol{H}^1_*(\mathcal{B}_2) \,|\, (\boldsymbol{v}_1)_n + (\boldsymbol{v}_2)_n \leq t\} \ ,$$

where $\boldsymbol{H}^1_*(\mathcal{B}_k) \subset \boldsymbol{H}^1(\mathcal{B}_k)$ satisfies homogeneous Dirichlet boundary conditions on $\partial\mathcal{B}_k \cap \Gamma_D$. To avoid confusion, we do not drop the dependency of the solution space on the body $\mathscr{B}_k$, $k = 1, 2$, respectively.

Then, the weak solution of (2.9) and (7.2) is defined by: Find $\boldsymbol{u} \in \mathcal{K}$ such that

$$\mathcal{J}(\boldsymbol{u}) \leq \min_{\boldsymbol{v}\in\mathcal{K}} \mathcal{J}(\boldsymbol{v}) \ , \tag{7.3}$$

where the energy functional $\mathcal{J}(\cdot)$ is given by $\mathcal{J}(\boldsymbol{v}) := \frac{1}{2}a(\boldsymbol{v},\boldsymbol{v}) - f(\boldsymbol{v})$ on $\mathcal{K}$, see, e.g., [HH80, BGK87]. The minimization problem (7.3) is equivalent to a variational inequality: Find $\boldsymbol{u} \in \mathcal{K}$ such that

$$a(\boldsymbol{u},\boldsymbol{v}-\boldsymbol{u}) \geq f(\boldsymbol{v}-\boldsymbol{u}), \qquad \boldsymbol{v} \in \mathcal{K} \ .$$

Our approach on the discrete level is based on a Neumann–Dirichlet algorithm and inexact solvers. In each step, a linear inhomogeneous Neumann problem has to be solved. This is done by standard multigrid techniques. Furthermore, a nonlinear one-sided contact problem has to be solved. Here, we use our monotone multigrid method introduced in Chapter 3. The information transfer at the contact boundary is realized in terms of the scaled mass matrix. The major advantages of this new approach are the efficiency of the iterative solver, and the a priori estimates for the boundary stresses at the actual contact zone. Introducing the boundary stress formally as Lagrange multiplier, the Neumann–Dirichlet formulation can be interpreted as a mortar setting. In contrast to penalty methods, the discretization error of the boundary stresses does not depend on regularization parameters. We recall that the Lagrange multiplicator is associated with the non-mortar side $\mathscr{B}_1$.

To motivate our approach, let us assume for the moment that the contact stress $\sigma_n$ is known on $\Gamma_S$. Then, problem (2.9)–(7.2) can be decoupled in the following way: In a first step, we solve an inhomogeneous Neumann problem on $\mathcal{B}_2$: Find $\boldsymbol{u}_2 \in \boldsymbol{H}^1_*(\mathcal{B}_2)$ such that

$$a_2(\boldsymbol{u}_2, \boldsymbol{v}) = f_2(\boldsymbol{v}) + (\sigma_n, v_n)_{\boldsymbol{L}^2(\Gamma_S)}, \qquad \boldsymbol{v} \in \boldsymbol{H}^1_*(\mathcal{B}_2) \ . \tag{7.4}$$

Having $\boldsymbol{u}_2 \in \boldsymbol{H}^1_*(\mathcal{B}_2)$, $\boldsymbol{u}_1 \in \boldsymbol{H}^1_*(\mathcal{B}_1)$ can be obtained in terms of $\boldsymbol{u}_{2|\Gamma_S}$. We define the convex set $\mathcal{K}(\boldsymbol{v}_2)$ of admissible displacements for a given $\boldsymbol{v}_2 \in \boldsymbol{H}^1_*(\mathcal{B}_2)$

$$\mathcal{K}(\boldsymbol{v}_2) := \{\boldsymbol{v}_1 \in \boldsymbol{H}^1_*(\mathcal{B}_1) \mid (\boldsymbol{v}_1)_n \leq t - (\boldsymbol{v}_2)_n \text{ on } \Gamma_S\} \ .$$

Then, the one-sided contact problem on $\mathcal{B}_1$ can be written as a variational inequality: Find $\boldsymbol{u}_1 \in \mathcal{K}(\boldsymbol{u}_2)$ such that

$$a_1(\boldsymbol{u}_1, \boldsymbol{v} - \boldsymbol{u}_1) \geq f_1(\boldsymbol{v} - \boldsymbol{u}_1), \qquad \boldsymbol{v} \in \mathcal{K}(\boldsymbol{u}_2) \ . \tag{7.5}$$

The discretization of the set $\mathcal{K}(\boldsymbol{v}_2)$ is given by

$$\mathcal{K}_j(\boldsymbol{v}_2) := \{\boldsymbol{v}_1 \in \boldsymbol{S}_1^{(j)} \,|\, (\boldsymbol{v}_1)_n(p) \leq t(p) - (\Pi \boldsymbol{v}_2)_n(p) \text{ for all } p \in \mathcal{P}_S\} \ ,$$

where $\boldsymbol{S}_k^{(j)}$ is the finite element space $\boldsymbol{S}^{(j)} \cap \boldsymbol{H}^1_*(\mathcal{B}_k)$, $k = 1, 2$, of vector valued piecewise linear hat functions on $\mathcal{B}_k$, cf. (2.27). $\mathcal{P}_S$ denotes the set of vertices onto the non-mortar side of $\overline{\Gamma}_S$, and $\Pi$ is a suitable mapping from the mortar side on the non-mortar side. In the conforming case where $\Pi = \mathrm{Id}$ is the standard choice, a priori estimates for the discretization error can be found in, e.g., [KO88]. We refer to [BHL97, BHL99] for an a priori analysis in the nonconforming case. Results on a posteriori error estimation for unilateral contact problems can be found in [CHP00]. Numerical examples for a mortar coupling with standard Lagrange multipliers in 2D without friction are given in [Hil00]. In the following, we do not use an additional index $j$ to denote the discrete approximation $\boldsymbol{u} = (\boldsymbol{u}_1, \boldsymbol{u}_2) \in \boldsymbol{S}_1^{(j)} \times \boldsymbol{S}_2^{(j)}$, and $\boldsymbol{\mu}$ stands for the discrete boundary stress. Here, in an abuse of notation, we do not distinguish between an element $\boldsymbol{v} \in \boldsymbol{S}^{(j)}$ and its vector representation with respect to the standard nodal basis. In addition, we identify the spaces $\boldsymbol{S}_k^{(j)}$ and $\mathbb{R}^{n_k}$, $n_k := \dim \boldsymbol{S}_k^{(j)}$, $k = 1, 2$. For $k = 1, 2$, we denote by $\boldsymbol{A}_N^k$ the stiffness matrix with respect to $a_k(\cdot, \cdot)$ and by $\boldsymbol{f}_k$ the vector associated with the right hand side.

The index $N$ of $\boldsymbol{A}_N^k$ indicates that the stiffness matrix corresponds to Neumann type boundary conditions at the interface. Before we formulate our algorithm, we consider the information transfer at the interface in more detail. We define the projection $\Pi$ in terms of the dual Lagrange multiplier space (6.10), whose definiton is taken from [Woh01]. Since here the situation is different, we recall the definition. Let $\lambda_p$, $p \in \mathcal{P}_S$, be the standard piecewise linear hat functions associated with the non-mortar side. Here, $N_S := \#\mathcal{P}_S$ stands for the number of vertices on the non-mortar side. For convenience, we recall the definition of the dual Lagrange multiplier space. We denote by $\psi_q$, $q \in \mathcal{P}_S$, a set of locally defined piecewise linear or bilinearbiorthonormal basis functions, i.e.,

$$\int_{\Gamma_S} \psi_q \lambda_p \; da = \delta_{pq}, p, q \in \mathcal{P}_S \;\; .$$

Moreover, we assume that $P_0(\Gamma_S) \subset \text{span}\,\{\psi_p, p \in \mathcal{P}_S\} =: M^j$.

We set $\Pi\colon \boldsymbol{S}_2^{(j)} \longrightarrow \boldsymbol{S}_1^{(j)}$,

$$(\Pi\; \boldsymbol{v})_i \;\; := \;\; \sum_{p \in \mathcal{P}_S} \int_{\Gamma_S} v_i \; \psi_p \; da \;\; \lambda_p \,, \quad \boldsymbol{v} \in \boldsymbol{S}_2^{(j)} \,, \quad 1 \leq i \leq d \;\; .$$

It is clear that $\Pi$ can also be applied to $\boldsymbol{v}_2 \in \boldsymbol{H}_*^1(\mathcal{B}_2)$. We denote the algebraic representation of $\Pi$ as function from $\mathbb{R}^{n_2}$ onto $\mathbb{R}^{n_1}$ by $\Sigma$, and we observe that $\Sigma$ is a $n_1 \times n_2$ matrix, which consists of large zero blocks and one non zero block associated with the vertices on the non-mortar and mortar side. Solving a discrete Dirichlet problem on $\mathcal{B}_1$ provides an approximation for the corresponding flux $\boldsymbol{\mu} \in \boldsymbol{M}^{(j)}$ on $\Gamma_S$. Within the mortar approach the discrete flux $\boldsymbol{\mu}$ is uniquely defined by

$$\int_{\Gamma_S} \boldsymbol{\mu} \; \boldsymbol{v} \, da = a_1(\boldsymbol{u}_1, \boldsymbol{v}) - f_1(\boldsymbol{v}), \quad \boldsymbol{v} \in \boldsymbol{S}_1^{(j)} \;\; .$$

Using $\boldsymbol{\mu} \in \boldsymbol{M}^{(j)}$ in (7.4), we find for an element $\boldsymbol{v}_2$ in $\boldsymbol{S}_2^{(j)}$

$$\int_{\Gamma_S} \boldsymbol{\mu} \; \boldsymbol{v}_2 \, da = \int_{\Gamma_S} \boldsymbol{\mu} \; \Pi \boldsymbol{v}_2 \, da = \int_{\Gamma_S} \Pi^* \boldsymbol{\mu} \; \boldsymbol{v}_2 \, da \;\; ,$$

where $\Pi^*$ denotes the adjoint operator of $\Pi$. The matrix representation of which is given by $\Sigma^T$. Here, we identify $\boldsymbol{M}^{(j)}$ with $\mathbb{R}^m$, $m := \dim \boldsymbol{M}^{(j)} \leq n_1$, and use the embedding $\mathbb{R}^m \subset \mathbb{R}^{n_1}$. Figure 7.1 illustrates the role of discrete transfer operators $\Sigma$ and $\Sigma^T$.

The transfer of the Dirichlet values at the contact boundary is realized in terms of the linear operator $\Pi$ and the transfer of the boundary stresses in terms of the adjoint operator, corresponding to the duality between displacements and stresses. In the algebraic formulation, the matrix $\Sigma$ is used to transfer the displacements on the mortar side as Dirichlet values, or more precisely as an obstacle, onto the non-mortar side, and the scaled boundary stresses are transferred from the non-mortar side to the mortar side in terms of the transposed matrix $\Sigma^T$. The interface conditions of the mortar formulation guarantee that (7.1) and (7.2) are satisfied in a weak integral form.

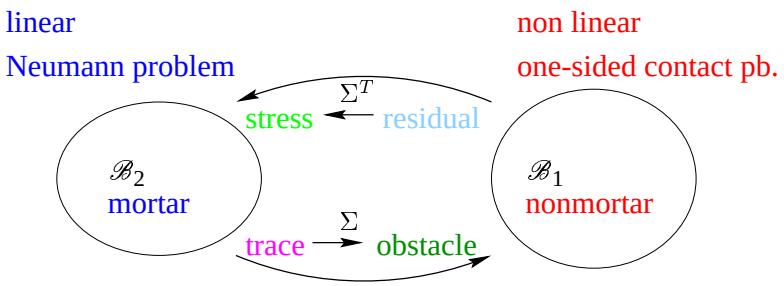


Figure 7.1: Discrete Dirichlet–Neumann coupling

## 7.1 Nonlinear Dirichlet–Neumann Algorithm

Now, our nonlinear Neumann–Dirichlet algorithm is defined in terms of $\boldsymbol{f}_1$, $\boldsymbol{f}_2$ and $\Sigma$:

**Algorithm 4**
Choose damping parameters: $0 < \eta_D, \eta_N \leq 1$.
Initialize: $\boldsymbol{S}_1^{(j)} \ni \boldsymbol{g}^0 = 0$, $\boldsymbol{S}_2^{(j)} \ni \boldsymbol{p}^1 = 0$.
For $\nu = 1, \ldots, N$ do

Solve linear Neumann problem: Find $\boldsymbol{u}_2^\nu \in \boldsymbol{S}_2^{(j)}$:

$$\boldsymbol{A}_N^2 \boldsymbol{u}_2^\nu \;=\; \boldsymbol{f}_2 - \boldsymbol{p}^\nu \;.$$

Transfer of the displacement and damping:

$$\boldsymbol{g}^\nu \;=\; (1-\eta_D)\boldsymbol{g}^{\nu-1} + \eta_D \Sigma \boldsymbol{u}_2^\nu \;.$$

Solve nonlinear one-sided contact problem: Find $\boldsymbol{u}_1^\nu \in \mathcal{K}_j(\boldsymbol{g}^\nu)$:

$$(\boldsymbol{A}_N^1 \boldsymbol{u}_1^\nu, \boldsymbol{v} - \boldsymbol{u}_1^\nu) \;\geq\; (\boldsymbol{f}_1, \boldsymbol{v} - \boldsymbol{u}_1^\nu), \qquad \boldsymbol{v} \in \mathcal{K}_j(\boldsymbol{g}_n^\nu) \;.$$

Compute the residual $\boldsymbol{r}_1^\nu \in \boldsymbol{S}_1^{(j)}$:

$$\boldsymbol{r}_1^\nu \;=\; \boldsymbol{A}_N^1 \boldsymbol{u}_1^\nu - \boldsymbol{f}_1 \;.$$

Transfer of the boundary stress and damping:

$$\boldsymbol{p}^{\nu+1} \;=\; (1-\eta_N)\boldsymbol{p}^\nu + \eta_N \Sigma^T \boldsymbol{r}_1^\nu \;.$$

In each step of our algorithm, we use a multigrid methods as solver. The variational inequality can be solved efficiently by our monotone multigrid methods introduced in Chapter 3.

Figure 7.2 illustrates the steps of our Neumann–Dirichlet algorithm for $\eta_D = 1$. On the left, the first step is shown. The choice $\boldsymbol{p}^1 = 0$ implies that a homogeneous Neumann problem has to be solved for $\boldsymbol{u}_2^1$. In the case that we have a full symmetric problem, it can be easily seen that the choice $\eta_N = 1$ does not yield a convergent scheme. The iterates oscillate between the two first iterates, i.e., $\boldsymbol{u}_2^{2m+1} = \boldsymbol{u}_2^1$, $\boldsymbol{u}_2^{2m+2} = \boldsymbol{u}_2^2$, $m \geq 1$.

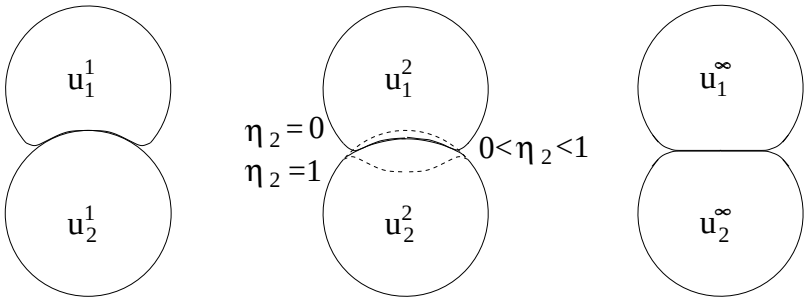


Figure 7.2: First iterates $(\boldsymbol{u}_1^1, \boldsymbol{u}_2^1)$ (left), second iterates (middle) and solution (right)

**Remark 7.1** *If the actual contact zone is known, the nonlinear contact problem will be linear. In this case, we can expect the same order of convergence as for a standard Neumann–Dirichlet type preconditioner for mortars, see [Dry99, Dry01].*

In the mortar setting, the Lagrange multiplier plays the role of Neumann boundary conditions. The combination of mortar finite elements, monotone multigrid methods and domain decomposition techniques defines in a natural way a new solution algorithm for elastic contact problems. The discrete boundary stress in the $\nu$-th iteration step $\boldsymbol{\mu}^\nu$ is the residual $\boldsymbol{r}_1^\nu$ restricted on $\Gamma_S$., Moreover, we obtain the normal stress $\sigma_n$ and the tangential stress $\sigma_T$ by a local rotation from the final $\boldsymbol{\mu}^\nu$. We remark, that our approach satisfies $\sigma_T = 0$, although we do not enforce this condition on the discrete space $\boldsymbol{M}^{(j)}$.

## 7.2 Numerical results

Finally, we present numerical examples for the proposed algorithm. Our numerical results can be found in [KW01]. Our first test problem is the Hertzian contact of a linear elastic circle with a linear elastic plane. In this example, the contact stresses can be computed analytically [Her82]. To test the performance of our algorithm, we compare the computed boundary stresses with the analytical ones. For comparability, we choose the same problem data and geometry as in [CSW99]. We consider an elastic circle with scaled material parameters $E = 7000$, $\nu = 0.3$ and radius $r = 1$, pressed by a point load $F = 100$ to a plane with material parameters $E = 10^6$, $\nu = 0.45$.

As is done in [CSW99], we apply the single load as surface load to avoid a singularity. We use bilinear functions on quadrilaterals. Figure 7.3 illustrates the performance of our method. In the left, the maximal contact stress on each level is given, in the middle the contact stresses and tangential stresses are shown, and in the right, the component $\sigma_{22}(\boldsymbol{u})$ of the stress tensor is depicted. The analytical value of $\sigma_n^{\max} = 495$ is already reached on level 5. Here, only 5 nodes of the circle are actual in contact with the plane. To demonstrate the flexibility of our approach, we do not enforce $\boldsymbol{\sigma}_T = 0$ on the space. The Lagrange multiplier of the mortar method plays the role of the boundary stresses at $\Gamma_S$. Thus, the boundary stresses are handled as additional unknowns which are obtained by restricting the residual. This observation predestinates our algorithm for contact problems with friction.

As long as the discrete contact boundary is not fully recognized, the convergence of

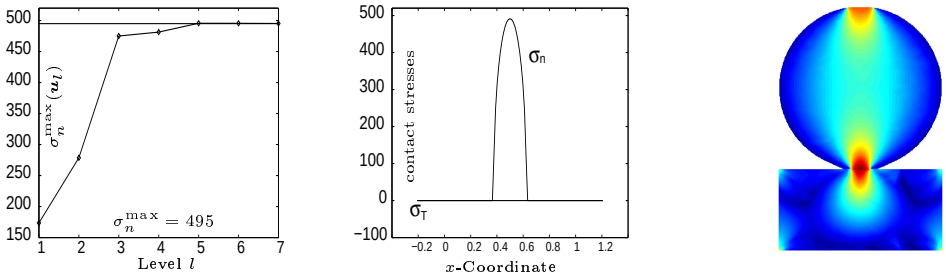


Figure 7.3: Maximal contact stresses (left), contact stresses (middle) and $\sigma_{22}$ (right)

the monotone multigrid method might be slow. This is due to the search for the contact boundary. In this example, the contact boundary is detected after at most three inner iterations, i.e., three iterations of the monotone multigrid method, and no slowdown occurs.

We define the stopping criteria for our iterative solver in terms of the Lagrange multiplier. Observing that the choice of our start vectors guarantees $\boldsymbol{A}_N^1 \boldsymbol{u}_1^n - \boldsymbol{f}_1 = 0$ for all interior nodes on $\mathcal{B}_1$, we find $\|(\boldsymbol{A}_N^1 \boldsymbol{u}_1^n - \boldsymbol{f}_1)_{\Gamma_S}\| = \|\boldsymbol{A}_N^1 \boldsymbol{u}_1^n - \boldsymbol{f}_1\|$. Moreover $\boldsymbol{p}^\nu$ can be interpreted as boundary stress on the mortar side in the $\nu$-th iteration step. This observation motivates our stopping criteria

$$\frac{\|\boldsymbol{p}^{\nu+1} - \boldsymbol{p}^\nu\|}{\|\boldsymbol{p}^\nu\|} \leq \mathrm{TOL} \frac{\|\boldsymbol{p}^3 - \boldsymbol{p}^2\|}{\|\boldsymbol{p}^2\|} \tag{7.6}$$

which is equivalent to $\|\boldsymbol{p}^\nu - \Sigma^T \boldsymbol{r}_1^\nu\|/\|\boldsymbol{p}^\nu\| \leq \mathrm{TOL}\|\boldsymbol{p}^2 - \Sigma^T \boldsymbol{r}_1^2\|/\|\boldsymbol{p}^2\|$. The use of the Euclidean vector norm is motivated by the mesh dependent norm $h\|\cdot\|^2_{\boldsymbol{L}^2(\Gamma_S)}$ for the Lagrange multiplier. We note that if the discrete boundary stress $\boldsymbol{p}$ is equal zero, then the contact problem is degenerated and two linear problems on $\mathcal{B}_1$ and $\mathcal{B}_2$ with homogeneous Neumann boundary conditions on $\Gamma_S$ have to be solved. In that case since $\boldsymbol{p}^1 = 0$, $\boldsymbol{g}^0 = 0$, we obtain the solution after one step. Moreover if $\boldsymbol{p} \neq 0$, $\eta_D = 1$ and $\boldsymbol{p}^{\nu_0} = 0$, $\nu_0 \geq 2$, the algorithm does not convergence and the damping parameter $\eta_N$ is too large. Table 7.1 shows the number of required iteration steps depending on the damping parameter and the refinement level. We set $\mathrm{TOL} = 10^{-4}$. If the damping parameters are small enough the number of required iteration steps can be bounded independently of the refinement level. Here we use uniform refinement on all levels. We observe a considerably smaller number of required iteration steps on Level 2 and Level 3 for $\eta_D = 1$ and $\eta_N = 0.4, 0.5$, see also Figure 7.5.

Figure 7.4 illustrates the influence of the choice of the damping parameters. The error reduction $g(\nu) := \|\boldsymbol{p}^{\nu+2} - \Sigma^T \boldsymbol{r}_1^{\nu+2}\| \, \|\boldsymbol{p}^2\|/\|\boldsymbol{p}^{\nu+2}\| \, \|\boldsymbol{p}^2 - \Sigma^T \boldsymbol{r}_1^2\|$ is shown versus the number $\nu$ of iteration steps. If the damping parameter is small enough, level independent upper bounds for the convergence rates can be observed.

Figure 7.5 illustrates the influence of small and too large damping factors. Small damping parameters lead to a slow convergence, see the left and middle picture in Figure 7.5. On the other hand, the algorithm does not converge for higher levels if the damping parameter is too large, see the right picture in Figure 7.5.

Table 7.1: Number of iteration steps, Lagrange multiplier norm

| | lev. 0 | lev. 1 | lev. 2 | lev. 3 | lev. 4 | lev. 5 | lev. 6 |
|---|---|---|---|---|---|---|---|
| $\eta_D = 1$, $\eta_N = 0.5$ | 11 | 11 | 5 | 6 | 13 | 10 | 12 |
| $\eta_D = 1$, $\eta_N = 0.4$ | 14 | 14 | 8 | 9 | 18 | 15 | 16 |
| $\eta_D = 0.5$, $\eta_N = 1$ | 12 | 11 | 6 | 6 | 6 | 8 | 11 |
| $\eta_D = 0.4$, $\eta_N = 1$ | 16 | 16 | 9 | 10 | 8 | 11 | 11 |
| $\eta_D = 0.6$, $\eta_N = 0.8$ | 9 | 8 | 8 | 9 | 7 | 8 | 9 |
| $\eta_D = 0.8$, $\eta_N = 0.6$ | 6 | 7 | 9 | 9 | 10 | 8 | 9 |
| $\eta_D = 0.7$, $\eta_N = 0.7$ | 8 | 7 | 10 | 9 | 9 | 8 | 9 |

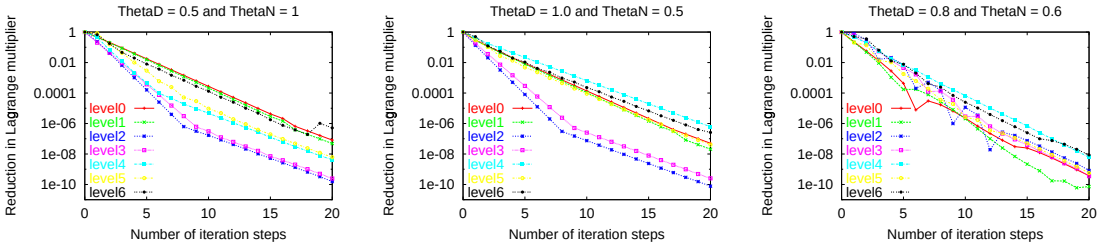


Figure 7.4: Error reduction for different damping parameters $\eta_N$, $\eta_D$

To be on the safe side, one has to chose a small damping factor. Unfortunately, the optimal damping parameter is in general not known. Adaptive strategies controlling the damping parameter might yield considerably better results. A different possibility to improve the performance is the use of our algorithm as preconditioner for a Krylov subspace method. As soon as the actual zone of contact is detected, we are in the linear setting. Then, our algorithm for $\eta_D = 1$ is equivalent to a preconditioned Schur complement system, and we can apply a conjugate gradient method.

In our next example, we consider the elastic contact of a wrench and a nut. At the interior boundary of the nut, i.e., the part of the boundary with outer normal pointing towards the center of gravity of the nut, we impose Dirichlet boundary conditions corresponding to a rotation. Homogeneous Dirichlet boundary conditions are applied at the

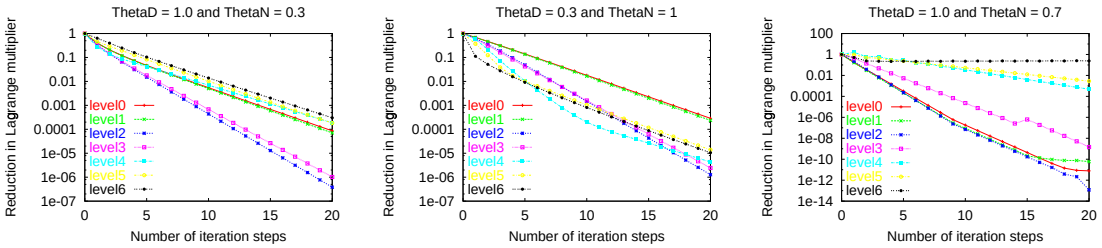


Figure 7.5: Influence of too small and too large damping parameters

handle of the wrench and on all remaining parts of the boundary we impose homogeneous Neumann conditions. We use linear elements on triangles, and refinement is done adaptively. As can be seen in the right of Figure 7.6, the actual contact zone is only a small part of the contact boundary $\Gamma_S$. We remark, that a more realistic model would include friction at the interface.

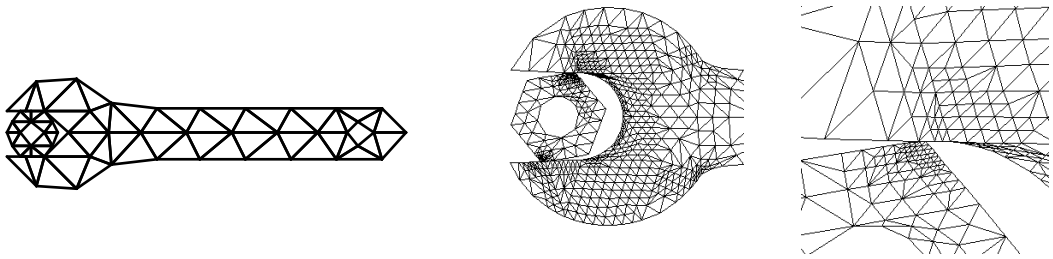

Figure 7.6: Initial triangulation (left), deformation and final triangulation (middle) and zoom at the contact zone (right)

## 7.3 Elastic Contact with Coulomb friction

In this section, we consider a nonlinear contact problem with Coulomb friction, see Chapter 6. The Coulomb law can be applied for two linear elastic bodies in contact if we replace the tangential displacement by the *relative* tangential displacement, see [IW92, Eck96]. Then, the equilibrium conditions at the contact boundary and the Coulomb's law reads as follows:

$$\begin{array}{ll} \boldsymbol{\sigma}_T(\boldsymbol{u}_1) = \boldsymbol{\sigma}_T(\boldsymbol{u}_2), & \sigma_n(\boldsymbol{u}_1) = \sigma_n(\boldsymbol{u}_2) \le 0 \ , \\ |\boldsymbol{\sigma}_T(\boldsymbol{u}_1)| \le \mathcal{F}|\sigma_n(\boldsymbol{u}_1)|, & \boldsymbol{\sigma}_T(\boldsymbol{u}_1)[\boldsymbol{u}_T] + \mathcal{F}|\sigma_n(\boldsymbol{u}_1)|\,|[\boldsymbol{u}_T]| = 0 \ , \end{array} \tag{7.7}$$

where $\mathcal{F} > 0$ is the friction coefficient and the jump is defined by $[\boldsymbol{u}_T] := (\boldsymbol{u}_1)_T - (\boldsymbol{u}_2)_T$. An equivalent formulation of Coulomb's law can be given by $|\boldsymbol{\sigma}_T(\boldsymbol{u}_1)| \le \mathcal{F}|\sigma_n(\boldsymbol{u}_1)|$ and

$$\begin{array}{llll} \text{if} & |\boldsymbol{\sigma}_T(\boldsymbol{u}_1)| < \mathcal{F}|\sigma_n(\boldsymbol{u}_1)| & \Longrightarrow & [\boldsymbol{u}_T] = 0 \\ \text{if} & |\boldsymbol{\sigma}_T(\boldsymbol{u}_1)| = \mathcal{F}|\sigma_n(\boldsymbol{u}_1)| & \Longrightarrow & [\boldsymbol{u}_T] = -s\boldsymbol{\sigma}_T(\boldsymbol{u}_1), \quad s \ge 0 \ ; \end{array}$$

see also [Has92, KB92]. Then, the equilibrium condition satisfies the boundary value problem given by (2.9), (7.2) and (7.7). As in the frictionless case, we base our numerical approach on the variational formulation. To do so, we use the principle of virtual work. As in Chapter 6, we use the nonlinear functional $\omega(\cdot,\cdot)$ to describe the virtual work of the frictional forces. Here, $\omega$ takes the form

$$\omega(\boldsymbol{u},\boldsymbol{v}) := \int_{\Gamma_S} \mathcal{F}|\sigma_n(\boldsymbol{u}_1)|\,|[\boldsymbol{v}_T]|\,da \ .$$

Following the lines of [KO88, Chapter 10], a variational inequality can be obtained from (2.9), (7.2) and (7.7) by applying Green's formula. The weak form of (2.9), (7.2) and (7.7)

reads as follows: Find $\boldsymbol{u} \in \mathcal{K}$ such that

$$a(\boldsymbol{u}, \boldsymbol{v}-\boldsymbol{u}) + \omega(\boldsymbol{u}, \boldsymbol{v}) - \omega(\boldsymbol{u}, \boldsymbol{u}) \geq f(\boldsymbol{v}-\boldsymbol{u}), \quad \boldsymbol{u} \in \mathcal{K} \ . \tag{7.8}$$

Moreover under suitable assumptions on the data, (7.8) and (2.9), (7.2) and (7.7) are equivalent, see [Eck96, Satz 1.6]. We do not address questions such as existence, uniqueness and regularity of a solution. Recently existence results for a large class of contact problems with friction have been obtained. We refer to [Eck96, EJ98, HHNL88, NJH80] and the references therein.

We follow, the lines of the previous paragraph to motivate our algorithm. Let us assume that the boundary stresses $\boldsymbol{\sigma}_T$ and $\sigma_n$ are known on the contact boundary. Then, the boundary value problem (2.9), (7.2) and (7.7) can be decoupled. The solution on $\mathscr{B}_N$ can be obtained as the solution of an inhomogeneous Neumann problem: Find $\boldsymbol{u}_2 \in \boldsymbol{H}^1_*(\mathscr{B}_N)$ such that

$$a_2(\boldsymbol{u}_2, \boldsymbol{v}) = f_2(\boldsymbol{v}) + (\sigma_n, \boldsymbol{v}_n)_{\boldsymbol{L}^2(\Gamma_S)}, + (\boldsymbol{\sigma}_T, \boldsymbol{v}_T)_{\boldsymbol{L}^2(\Gamma_S)} \qquad \boldsymbol{v} \in \boldsymbol{H}^1_*(\mathscr{B}_N) \ .$$

To obtain $\boldsymbol{u}_1$, we solve a nonlinear one-sided contact problem with Coulomb friction on $\mathcal{B}_1$. Then, the variational inequality (7.8) reduces to $\boldsymbol{u}_1 \in \mathcal{K}(\boldsymbol{u}_2)$

$$a_1(\boldsymbol{u}_1, \boldsymbol{v}-\boldsymbol{u}_1) + \omega_{\sigma_n;\boldsymbol{u}_2}(\boldsymbol{v}) - \omega_{\sigma_n;\boldsymbol{u}_2}(\boldsymbol{u}_1) \geq f_1(\boldsymbol{v}-\boldsymbol{u}_1), \quad \boldsymbol{v} \in \mathcal{K}(\boldsymbol{u}_2) \ ,$$

where the reduced form of the virtual work for a given function $\tau$ and a given displacement $\boldsymbol{w}$ is defined by

$$\omega_{\tau,\boldsymbol{w}}(\boldsymbol{v}) := \int_{\Gamma_S} \mathcal{F}\,|\tau|\,|\boldsymbol{v}_T - \boldsymbol{w}_T|\,da \ . \tag{7.9}$$

Now, we proceed as in the previous paragraph and carry out a fixed point iteration. Our nonlinear Neumann–Dirichlet algorithm for a contact problem with Coulomb friction reads as:

**Algorithm 5**
Choose damping parameters: $0 < \eta_D, \eta_N \leq 1$.
Initialize: $\boldsymbol{S}_1^{(j)} \ni \boldsymbol{g}^0 := 0$, $\boldsymbol{S}_2^{(j)} \ni \boldsymbol{p}^1 := 0$.
For $\nu = 1, \ldots, N$ do

Solve linear Neumann problem: Find $\boldsymbol{u}_2^\nu \in \boldsymbol{S}_2^{(j)}$:

$$\boldsymbol{A}_N^2 \boldsymbol{u}_2^\nu \quad = \quad \boldsymbol{f}_2 - \boldsymbol{p}^\nu \ .$$

Transfer of displacements and damping:

$$\boldsymbol{g}^\nu \quad = \quad (1-\eta_D)\boldsymbol{g}^{\nu-1} + \eta_D \Sigma \boldsymbol{u}_2^\nu \ .$$

Solve nonlinear one-sided contact problem with Coulomb friction:
Find $\boldsymbol{u}_1^\nu \in \mathcal{K}_j(\boldsymbol{g}^\nu)$:

$$(\boldsymbol{A}_N^1 \boldsymbol{u}_1^\nu, \boldsymbol{v}-\boldsymbol{u}_1^\nu) + \boldsymbol{\omega}_{(\boldsymbol{r}_1^\nu)_n;\boldsymbol{g}^\nu}(\boldsymbol{v}) - \boldsymbol{\omega}_{(\boldsymbol{r}_1^\nu)_n;\boldsymbol{g}^\nu}(\boldsymbol{u}_1^\nu) \quad \geq \quad (\boldsymbol{f}_1, \boldsymbol{v}-\boldsymbol{u}_1^\nu), \quad \boldsymbol{v} \in \mathcal{K}_j(g_n^\nu) \ .$$

Compute the residual $\boldsymbol{r}_1^\nu \in \boldsymbol{S}_1^{(j)}$:

$$\boldsymbol{r}_1^\nu \quad = \quad \boldsymbol{A}_N^1 \boldsymbol{u}_1^\nu - \boldsymbol{f}_1 \ .$$

Transfer of scaled boundary stresses and damping:

$$\boldsymbol{p}^{\nu+1} \quad = \quad (1-\eta_N)\boldsymbol{p}^\nu + \eta_N \Sigma^T \boldsymbol{r}_1^\nu \ .$$

Here, $\boldsymbol{\omega}_{\cdot;\cdot}(\cdot)$ is the algebraic representation of the nonlinear functional $\omega_{\cdot;\cdot}(\cdot)$ defined by (7.9).

## 7.4 Numerical Results with Coulomb friction

In this section, we present some numerical results in 2D and 3D illustrating the influence of the Coulomb friction on the deformation. These examples can be found in [KW01]. In all our 2D results, the friction coefficient is $\mathcal{F} = 0.3$. We start with the Hertz problem of Section 7.2. Figure 7.7 shows the boundary stresses at the contact zone. The initial triangulation has four elements on each subdomain.

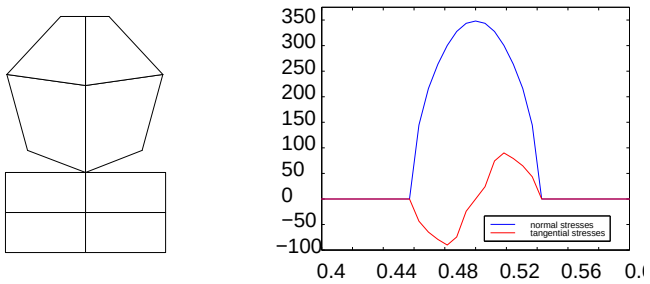


Figure 7.7: Initial triangulation (left) and boundary stresses (right)

Comparing Figure 7.7 with Figure 7.3, we find that the actual zone of contact and the maximal normal stress are considerably smaller if Coulomb friction occurs. Between the minimum and the maximum of the tangential stress no sliding occurs at the contact zone. Sliding nodes can be found in the neighborhood of the left and right endpoints of the actual contact.

As a second example in 2D we consider a symmetric problem. Here due to the symmetry, we expect that the tangential stress is zero even if friction terms are included. Figure 7.8 shows the boundary stress for the frictionless case and for the case including Coulomb friction. Comparing the left and right picture in Figure 7.8, we find exactly the same values for the normal stress and thus the actual zone of contact.

In contrast to the unsymmetric problem in Figure 7.7, no tangential stress occurs. Since the normal and tangential stress is the same at $\Gamma_S$, the discrete solutions for the two situations are the same. Figure 7.9 illustrates the stress component $\sigma_{22}$ close to the contact zone. Although our Dirichlet Neumann algorithm is non symmetric, we obtain a symmetric numerical approximation. The numerical results confirms the flexibility and reliability of the non-conforming approach in terms of dual Lagrange multipliers.

In our last example, we consider the elastic contact of three bodies in 3D. Two cylinders are in contact with a hexahedral bar. At the top and bottom of the upper and lower

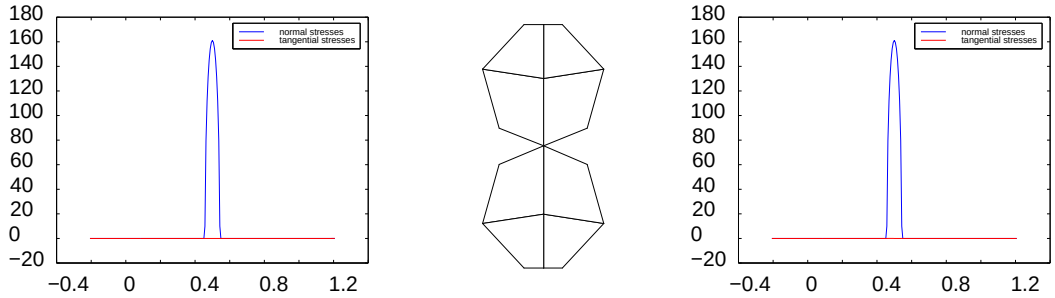


Figure 7.8: Boundary stresses (frictionless) (left), initial triangulation (middle) and boundary stresses (Coulomb friction) (right)

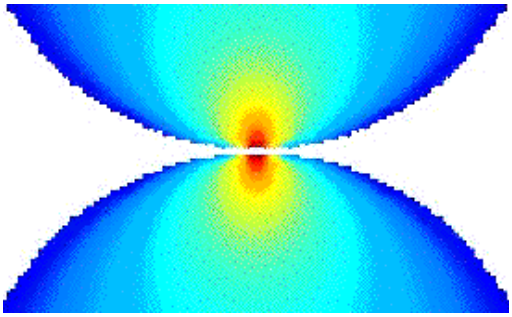

Figure 7.9: Boundary stress $\sigma_{22}$

cylinder, respectively, a displacement in vertical direction towards the bar is enforced. As before in 2D, we start with a very coarse initial triangulation, see Figure 7.10. On Level 0, we only have 5 elements. We use a standard mean value adaptive refinement strategy. The local refinement is controlled by a residual based local a posteriori error indicator on the subdomains and the information transfer at the interface is realized by additional terms in the definition of the local error indicator. On the non-mortar side the local jump $1/h\|[\boldsymbol{u}]\|^2_{\boldsymbol{L}^2(\Gamma_S)}$ measures the non-conformity which controls the discrete non-penetration condition. On the mortar side, we add locally the term $h\|[\boldsymbol{\mu}]\|^2_{\boldsymbol{L}^2(\Gamma_S)}$ which controls the discrete equilibrium condition for the stress at the contact boundary. The local weights $1/h$ and $h$ reflect the duality between the $H^{1/2}$ and $H^{-1/2}$ spaces. In contrast to conforming methods, no refinement rules have to be considered at the interfaces.

In the right picture in Figure 7.10 a cut of the adaptive triangulation on Level 7 is depicted, showing the meshes in the interior of the computational domain. We observe strong refinement in the neighborhood of the contact zone. Instead of $10,485,760$ elements in the case of uniform refinement, we have $207,561$ elements on Level 7. Using a coefficient of friction of $\mathcal{F} = 0.25$, we obtain 210 non-mortar nodes in contact on the finest level and 186 sticky nodes. We note, that no element at the interface has been refined within the last refinement step.

The asymptotic convergence rate of our algorithm depends highly on the aspect ratio of the hexahedral bar. It can be improved by using the proposed algorithm as a preconditioner within a Krylov subspace method. Finally, Figure 7.11 shows the coefficients with

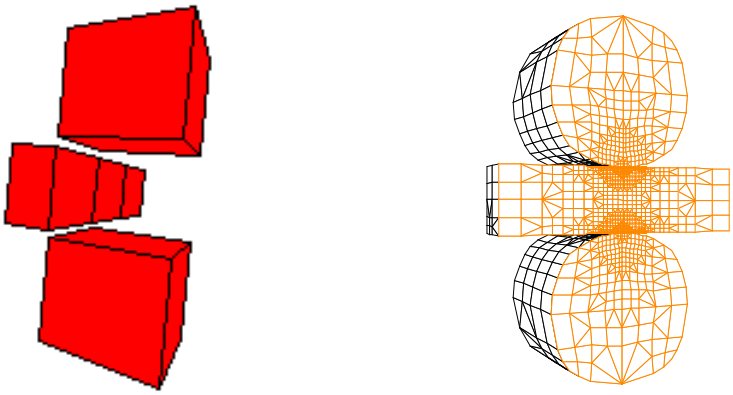

Figure 7.10: Initial (left) and adaptive (right) triangulation of a three body contact problem in 3D

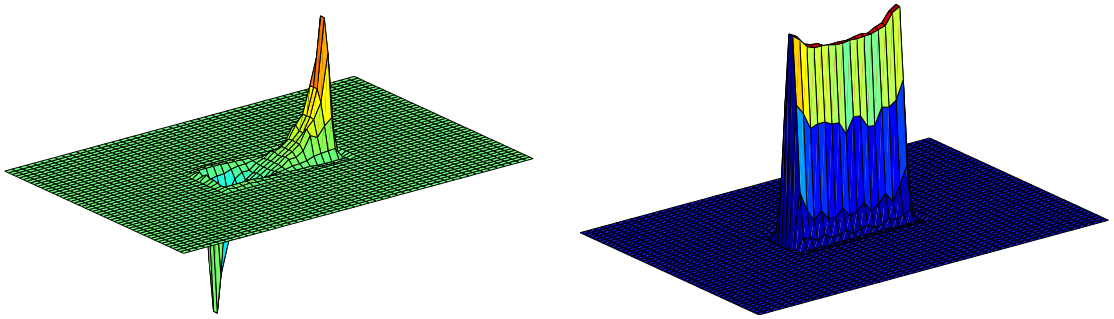

Figure 7.11: Tangential (left) and normal (right) stress at one of the interfaces

respect to the dual basis of the stress in normal direction and of one stress component in tangential direction. The second tangential component is of smaller size. The contact stresses are depicted with respect to the surface of the upper cylinder. This choice is arbitrary, since the problem is symmetric with respect to the symmetry plane of the two cylinders. Since the width of the cylinder in direction of the axis of the cylinder is larger than the width of the bar, the normal stress is zero at the part of the cylinder's surface being on the left and right of the bar, respectively. The tangential stresses increase until their norm reaches the critical value $\mathcal{F}|\sigma_n|$. Then, sliding occurs in opposite direction to the tangential stresses. All node on the contact boundary lying in between the minimum and maximum of the tangential stresses are sticky nodes, all others are sliding nodes.